A Novel Compact Fractal Ring Based Cylindrical Dielectric Resonator Antenna for Ultra Wideband Application

Dileep Sankaranarayanan*, **Duggirala Venkatakiran, and Biswajeet Mukherjee**

Abstract—This paper presents a novel compact Koch snowflake fractal ring based Dielectric Resonator Antenna (DRA) for ultra wideband application. Firstly, Koch snowflake fractal geometry is implemented on the conventional Cylindrical Dielectric Resonator Antenna (CDRA). Further, the performance of the DRA is enhanced by fractal ring created on the snowflake geometry. With the application of the fractal and the fractal ring geometry, the Q-factor of DRA is reduced, thus the bandwidth of DRA is increased. The proposed antenna offers a wide impedance bandwidth of 90% ranging from 4.7 GHz–12.4 GHz. The effect of the fractal geometry enhances the gain of DRA. The proposed antenna achieves radiation efficiency more than 78%, throughout the bandwidth. Interestingly, the proposed configuration reduces the DRA volume by 76.63% with reduced volume of 7.91 cm^3. The experimental verification of the proposed structure shows good agreement between simulated and measured results.

1. INTRODUCTION

In recent times, Dielectric Resonator Antenna (DRA) has witnessed huge attention due to its high radiation efficiency and wide impedance bandwidth. There have been rigorous investigations carried out on different geometries of DRA. The first DRA derived on cylindrical geometry was under the assumption of dielectric resonator not enclosed by conductor boundary will radiate. This was credited to Long [1]. This simple structure offered several advantages such as low cost and ease of machining. Unlike patch antenna, DRA does not support propagation of surface waves. This makes it efficient for high frequency applications [2].

A dielectric resonator has 3-dimensional geometry. It enhances the flexibility of design. Most common geometries of DRA are rectangular, hemispherical, and triangular [3, 4]. Each geometry has different radiation characteristics. The mode of DRA depends on the geometry and feeding method. There are different ways to excite DRA. The type of coupling scheme and its location with respect to the antenna can affect its performance in terms of impedance bandwidth, radiation patterns and gain. Coaxial probe, coplanar waveguide, microstrip and aperture coupling methods are most common coupling schemes of DRA [2]. Several methods have been proposed for bandwidth enhancement of DRA. The inclusion of fractals puts a new insight into them. Fractals are self-similar and repetitive complex patterns [5]. The fractal structure offers wide impedance bandwidth which has been reported on rectangular, cylindrical and hemispherical DRAs [6, 7]. Stacked DRA, dual-segment, hybrid DRA and slots in ground plane also well suited for improving the impedance bandwidth of DRA [8–12]. However, this makes the antenna bulky and less compact. Annular ring geometry is another way to increase the bandwidth of DRA. This will impart weight reduction too. In [13], Minkowski fractal DRA with a cylindrical hole provides enhanced bandwidth and gain.

This paper analyses the bandwidth enhancement of CDRA by Koch snowflake fractal ring. Initially, a conventional CDRA is designed, and snowflake geometry is applied to it. Koch snowflake fractal DRA implemented on CDRA offers wide impedance bandwidth and high gain. This is due to increase in surface area of DRA by the application of the fractal geometry. The bandwidth of Koch snowflake fractal DRA is further increased by removing a small size Koch snowflake geometry from the central portion of DRA. Removing a portion of dielectric material from DRA reduces the permittivity and increases the surface area to volume ratio (S/V); hence the Q-factor of DRA is also lowered. Finally, the structure is made compact by removing a half portion of DRA. A prototype based on optimized dimension is fabricated and experimentally verified.

2. KOCH SNOWFLAKE

Koch snowflake is generated from a simple Koch curve. A Koch curve is created by dividing a line segment into three equal parts. The middle segment forms base of the equilateral triangle. Thus, the base of the triangle is eliminated to create the subsequent fractals. Figure 1(a) shows an equilateral triangle T_1 with side S. For the first iteration, an equilateral triangle T_2 with length 1/3rd of the length of T_1 is created and placed along each of the three sides of T_1 towards the outer periphery as shown in Figure 1(b). In the second iteration, the equilateral triangle is placed with 1/9th of the original length of T_1 triangle, and the process is continued to obtain higher order iterations [5, 14].
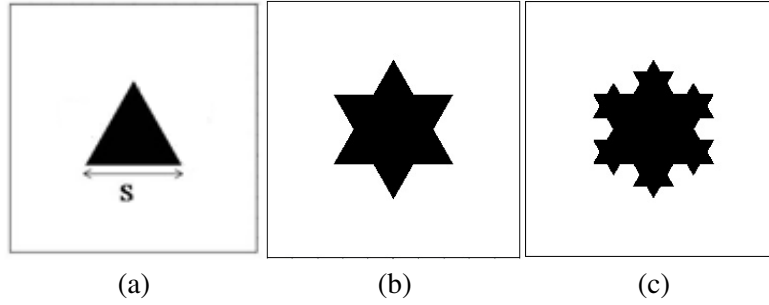
Figure 1. (a) T_1: equilateral triangle with side S. (b) T_2: first iteration. (c) T_3: second iteration.

Fractals are self-similar and repetitive patterns, thus its dimensions are different from lines, curves and planes. The dimension of a Koch snowflake is calculated by using self-similar property of fractal in terms of Hausdroff dimension. During each of the iterations, the number of sides of the Koch snowflake is increased by 4 times with side length 1/3 of the original one. The dimension of Koch snowflake is given as mentioned below [15, 16],

$$\text{Dim} = \lim_{n \to \infty} \frac{\ln(4^n)}{\ln(3^n)} = \frac{\ln(4)}{\ln(3)} \approx 1.2619 \tag{1}$$

The total number of sides (N) of Koch snowflake after n iterations is given by,

$$N = 3 * 4^n \tag{2}$$

The equilateral triangle has sides of length S, and the length of each side of the snowflake after n iteration

$$S_n = \frac{S}{3^n} \tag{3}$$

The perimeter (P) after n-iteration is given by,

$$P = 3 * S * \left(\frac{4}{3}\right)^n \tag{4}$$

3. ANTENNA CONFIGURATION

The antenna configuration is described in the following subsections. The first section presents conventional CDRA design and its simulated S_{11} results. The second section focuses on implementation of Koch snowflake fractal geometry on conventional CDRA and its parametric studies. Further, the comparison of its performance for various iterations and optimized parameters calculated are also shown. The third section proposes annular ring geometry on the optimized geometry from the second section and its parametric studies. The final section explains the compact structure made from the fractal ring. All simulations have been done on CST Microwave Studio 2014 by keeping 25 mesh cells per wavelength.

3.1. CDRA Design

The dimensions of the conventional CDRA are calculated for resonating at 3.8 GHz using a magnetic wall model [2]. The radius and height of the CDRA are $a = 2.68$ cm and $h = 1.5$ cm. The antenna is designed on an FR4 material with relative permittivity $\varepsilon_r = 4.3$ and loss tangent $\tan\delta = 0.025$ placed on a large ground plane of 10 cm $\times$ 10 cm. It is excited by a 50 ohm coaxial probe of length, $l = 0.9$ cm kept at the center. The DRA resonates at 3.8 GHz with a bandwidth of 15% ranging from 3.56 GHz–4.12 GHz with 4.8 dBi gain at 3.8 GHz.
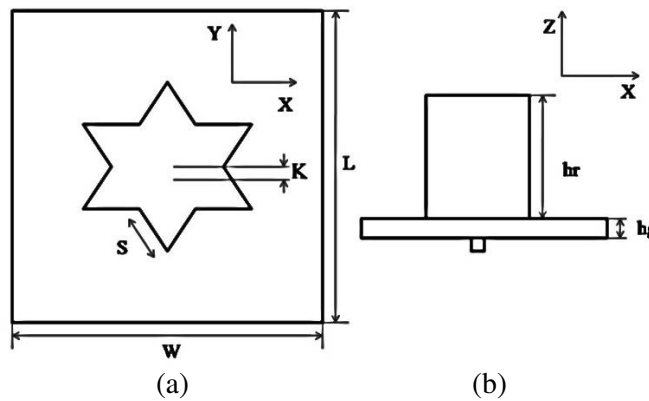

Figure 2. The structure of antenna. (a) Top view. (b) Front view. W and L are the length and width of ground plane, $W = L = 10$ cm. $K = 0.5$ cm is the distance from center to the probe, hr and hg are the height of resonator and ground plane with $hr = 1.5$ cm and $hg = 0.1$ cm.
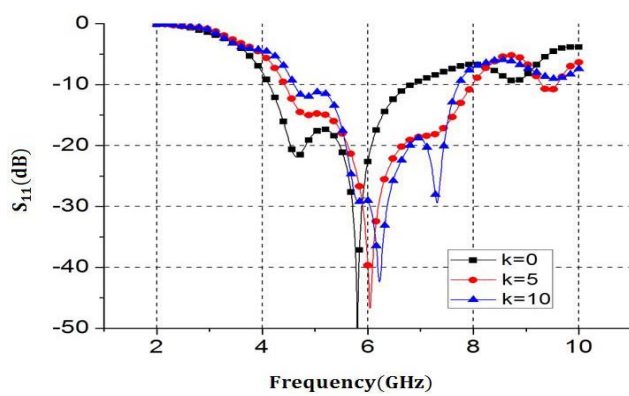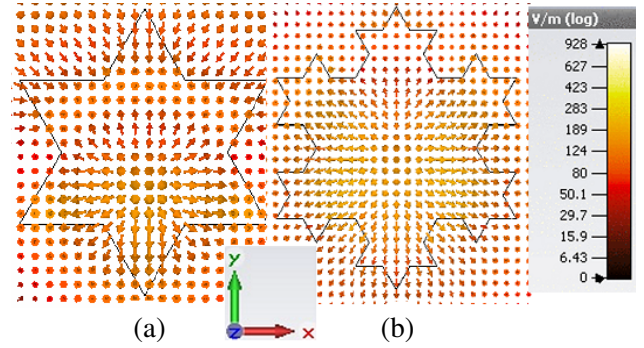

Figure 3. Simulated S_{11} plot of Koch snowflake first iteration at different probe positions (k).
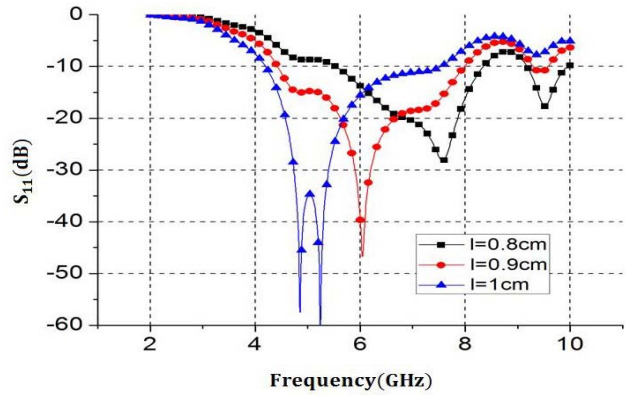
Figure 4. Simulated S_{11} plot of koch snowflake first iteration at different probe lengths.
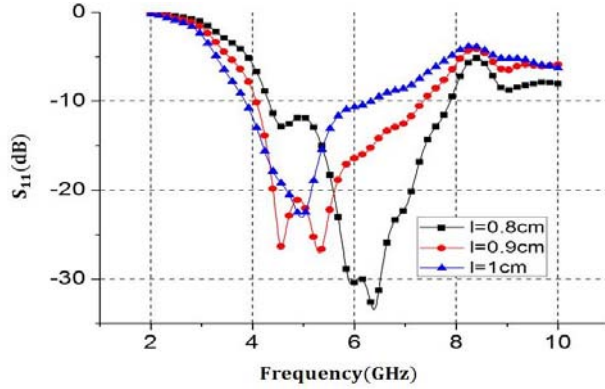
Figure 5. Simulated S_{11} plot of koch snowflake second iteration at different probe lengths (l).

Figure 6. Electric field distribution of Koch snowflake DRA on XY-plane. (a) First iteration at 6.04 GHz. (b) Second iteration at 4.57 GHz.

3.2. Koch Snowflake

On the CDRA, Koch snowflake fractal geometry is implemented up to two iterations as shown in Figures 1(a) and (b). The length of each side in iteration 1 is 15.6 mm, while in iteration 2 it is reduced to 5.2 mm. Number of sides in the first iteration is 12, and it is increased to 48 in iteration 2. Iteration 1 covers a perimeter of 62.4 mm, and iteration 2 covers 83.2 mm based on Equation (4). With increasing number of iterations, the fractal structure tries to form a curve with large perimeter.

Figure 2 shows the top and front views of the first iteration of the fractal DRA. From Figure 2, it can be seen that S is the side length (i.e., $S = 15.6$ mm) and K the distance between the position of probe from the center of the Koch snowflake DRA along Y-axis. The simulated S_{11} plot of Koch snowflake first iteration for different probe positions along Y-axis is shown in Figure 3. The position of the probe has varied from $K = 0$ cm to $K = 0.5$ cm. As moving away from the center of DRA, the resonant frequency shifts more towards the higher frequency, and impedance bandwidth increases. The position of the probe, $K = 0.5$ cm from the center of DRA, gives a better impedance bandwidth by the perfect impedance matching. Further increasing the value of K from $K = 0.5$ cm to $K = 1$ cm, the bandwidth of the DRA decreases. The optimized probe location is $X = 0$ cm and $Y = -0.5$ cm.

After optimizing the position of iteration 1, the length of probe is varied from $l = 0.8$ cm to $l = 1$ cm. Figure 4 shows the S_{11} plot of snowflake first iteration for different probe lengths. As the length of the probe increases the coupling to the DRA also increases, thus the resonant frequency of the DRA is decreased. It is evident that wide bandwidth is observed at $l = 0.9$ cm. The DRA resonates at 6.04 GHz with bandwidth 57.2% in the range of 4.43 GHz–7.98 GHz with a gain of 5.9 dBi. From the parametric studies, the probe length is optimized for effective impedance matching, and the optimized probe length is $l = 0.9$ cm.

In order to improve impedance bandwidth further, the second iteration is applied. The length of the probe is varied for improving the impedance matching. The parametric results of the fractal in the second iteration are shown in Figure 5. The optimized probe length is $l = 0.9$ cm. As can be seen, in the second iteration the resonant frequency decreases compared to the first iteration. This is due to the increase in volume of DRA with the increase in the iteration. The snowflake iteration 2 resonates at 4.57 GHz with a bandwidth of 57.6% (4.07–7.36) GHz with 6.57 dBi gain. Compared to iteration 1, iteration 2 covers more surface area, which increases the gain of the DRA.

The electric field distributions of the snowflake for various iterations at the respective resonant frequencies are shown in Figure 6(a) and Figure 6(b). The coaxial probe excites the DRA at an offset position, as the position of the probe has kept at an offset distance from the center. The electric fields are generated at $K = 0.5$ cm and distributing inside the dielectric resonator. The field distributions of the fractal structure are similar to the $TM_{01\delta}$ mode of CDRA [17].

Figure 7 shows the comparison of S_{11} plot of Koch snowflake for the first three iterations. It reveals
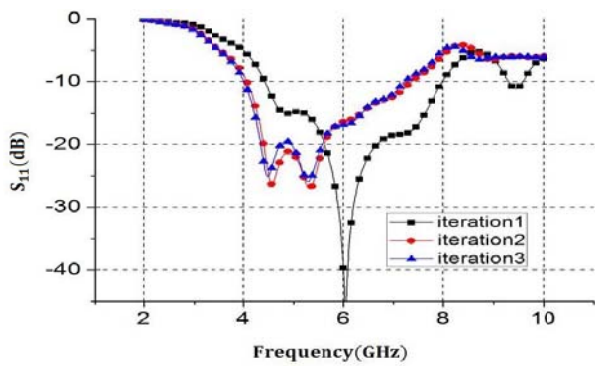
Figure 7. Simulated S_{11} plot of Koch snowflake iteration comparison.

(a)   (b)
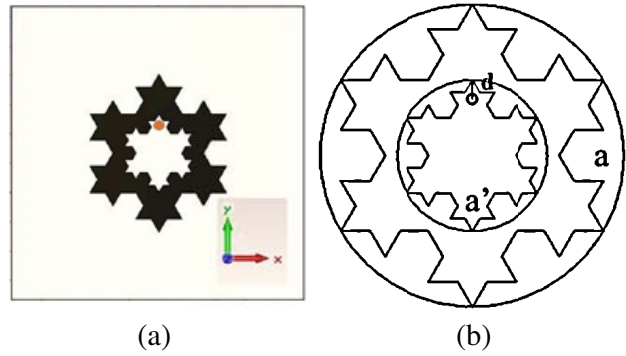
Figure 8. Top view of (a) fractal ring DRA, (b) fractal ring inside the annular ring.

that compared to the first iteration, the second iteration has a different resonant frequency, due to the difference in surface area of the two iterations. The S_{11} plots of iteration 2 and iteration 3 are similar. As can be seen, bandwidths offered by the second and third fractal iterations offer almost the same bandwidth. This is because the perturbation effects caused by the second and third iterations of the Koch snowflake are similar. Thus further analysis is carried out on the second iteration only to avoid any complex structure.
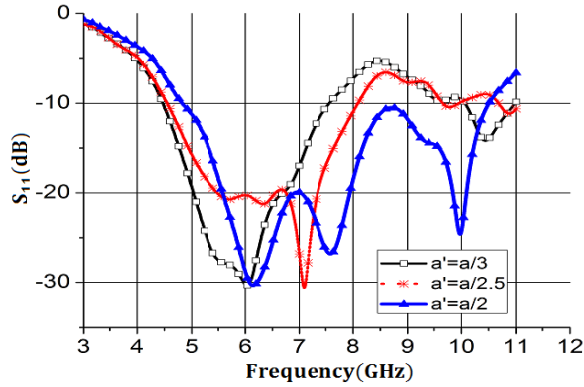
3.3. Annular Ring

The Koch snowflake fractal ring geometry is created by removing a similar fractal shaped section from the center of the fractal DRA. The creation of the annular ring symmetrically creates a slot in the DRA structure, thus reducing the effective permittivity and improving the bandwidth. The bandwidth of the fractal ring geometry can be varied by adjusting the diameter of the hole. The top view of the fractal ring DRA is shown in Figure 8(a), and Figure 8(b) shows the top view of annular ring geometry on an annular ring CDRA. In Figure 8(b), a represents the outer diameter of the ring, a' the inner diameter of the ring and 'd' the distance from the top edge of inner cylinder to the center of the probe ($d = 0.35$ cm).

Figure 9 shows the simulated S_{11} plot of the fractal ring DRA for various radii, where a' is the radius of the fractal hole. The value of a' is varied from $a/3$ to $a/2$. The dimension of $a' = a/3$ offers an impedance bandwidth of 3.16 GHz (52.84%) in the range of 4.4 GHz–7.56 GHz. Further, the value of a' is increased to $a' = a/2.5$. This offers an impedance bandwidth of 3.6 GHz (57.14%) ranging from 4.5 GHz to 8.5 GHz. The dimension of fractal hole is again increased to $a' = a/2$, and the DRA offers an impedance bandwidth of 5.69 GHz (74.23%). It can be observed that the wide bandwidth is obtained when the radius of the hole is half of the radius of the snowflake DRA. With increasing the dimension of the hole, the bandwidth is increased, and the resonant frequency is shifted towards the higher frequency side of the spectrum.

The variation of probe length of fractal ring is shown in Figure 10. As the probe length is increased from $l = 1$ cm, the bandwidth of DRA increases. At $l = 1.1$ cm, maximum impedance bandwidth is obtained. By further increasing the probe length, the impedance bandwidth is reduced. The best impedance matching is obtained for a probe length of $l = 1.1$ cm offering a wide impedance bandwidth of 5.69 GHz (74.23%) ranging (4.82–10.51) GHz with 7.6 dBi gain.

The electric field distribution of the fractal ring DRA at resonance is shown in Figure 11. It is similar to the $TM_{01\delta}$ mode of conventional CDRA [17]. The concentration of electric field lines is more in the upper half region of fractal ring DRA (section closer to the probe side), and very few field lines are concentrated in the lower region of DRA. Thus, the lower half can be removed from the proposed geometry. This aids in making the DRA physically small, however, retaining the same bandwidth of operation.

Figure 9. Simulated S_{11} plot of fractal ring for different radius.
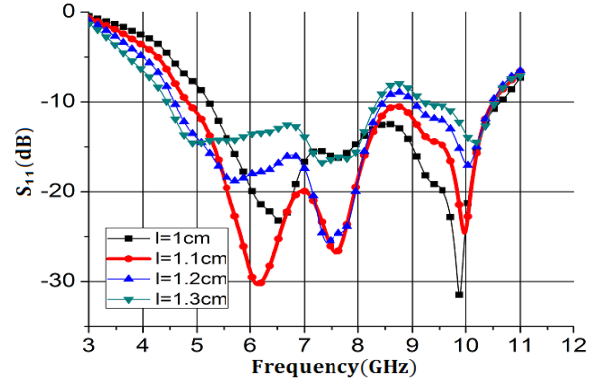
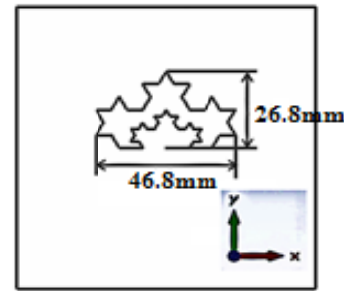**Figure 10.** Simulated S_{11} plot of fractal annular ring for different probe length (l).
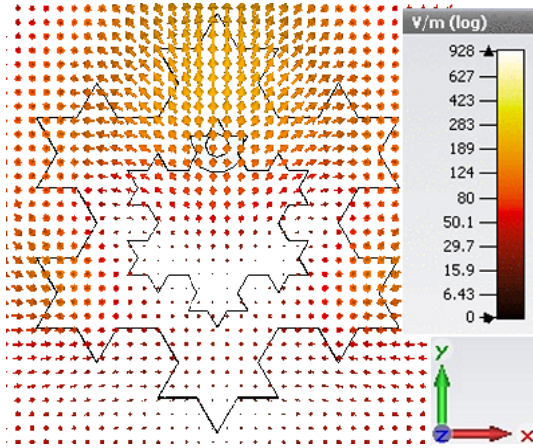
Figure 11. Electric field distribution of fractal ring DRA at 6.14 GHz on XY-Plane.

**Figure 12.** Top view of half split fractal ring DRA.

3.4. Half Split Annular Ring

In order to get the optimal design, the annular ring geometry is cut by half, and its parametric studies are carried out. Figure 12 shows the top view of the half split fractal ring DRA with dimensions.

Figure 13 shows the simulated S_{11} plot of half split fractal ring for various probe lengths. The probe length is varied from 1 cm to 1.3 cm. As the probe length is increased from $l = 1$ cm to $l = 1.2$ cm, the impedance bandwidth increases. Further increasing probe length from $l = 1.2$ cm to $l = 1.3$ cm, the impedance matching between the probe and the DRA is decreased. Hence the impedance bandwidth is decreased. It can be seen that DRA achieves the widest bandwidth when probe length $l = 1.2$ cm. It can be observed that a half split structure gives a better impedance bandwidth than a complete fractal ring. The simulation result shows the bandwidth of 6.09 GHz (4.6–10.69 GHz) with Peak gain of 9.13 dBi.

The electric field distribution of the half split fractal ring DRA is shown in Figure 14. The field distribution of a half split ring at lower frequency 6 GHz and 7.4 GHz is similar to $TM_{01\delta}$ like mode of CDRA [17].

Figure 15 shows the comparison of S_{11} plot of cylindrical ring DRA with the fractal ring and half split fractal ring. It can be seen that the fractal ring has better performance than conventional cylindrical ring DRA. From Figure 8(b), it can be inferred that the fractal ring covers more surface area and less volume than the annular ring DRA. Hence it offers more impedance bandwidth than annular ring DRA. The annular ring DRA offers an impedance bandwidth of 3.48 GHz (53.54%) in
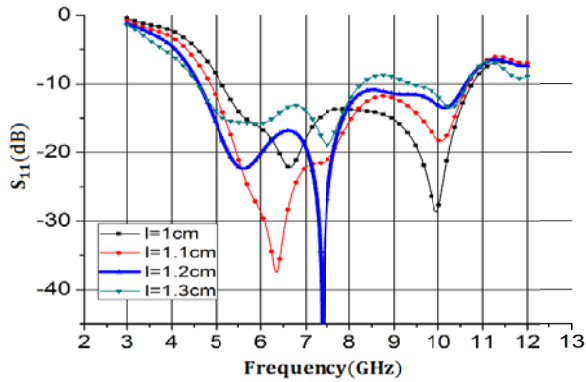
Figure 13. Simulated S_{11} plot of half split koch snowlake DRA for different probe length (l).
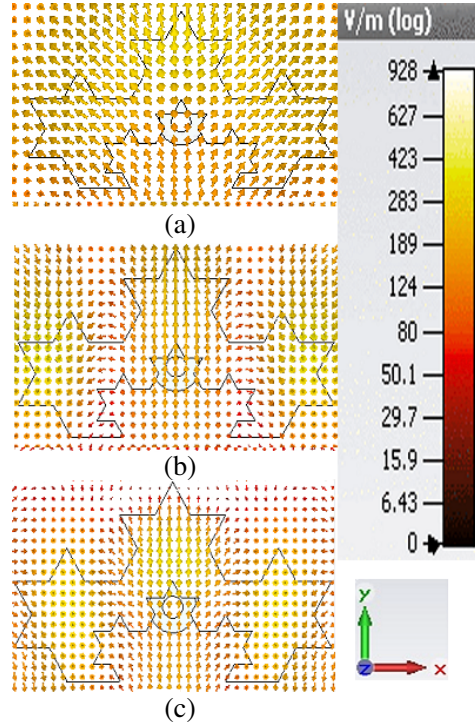
Figure 14. Electric field distribution of proposed configuration at (a) 6 GHz on XY-Plane. (b) Proposed configuration at 7 GHz on XY-Plane. (c) Proposed configuration at 10 GHz on XY-Plane.
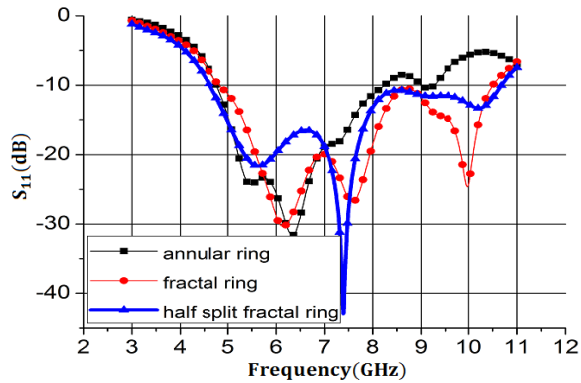
Figure 15. Simulated S_{11} plot of comparison.
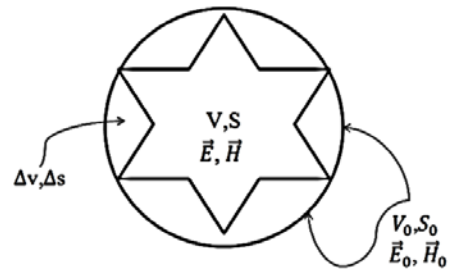
Figure 16. Cavity perturbation on CDRA edges by Koch snowflake fractal first iteration.

the frequency range of 4.76 GHz–8.24 GHz. However, the fractal ring offers an impedance bandwidth of 5.69 GHz (74.23%), which is 20.69% higher than that of annular ring DRA. It is noted that after removing a half portion of the fractal ring structure, the half split portion covers more impedance bandwidth due to the increase in surface area to volume ratio (S/V). The fractal ring has an S/V ratio of 4.21 while the half split fractal ring has 4.51. The half split fractal ring DRA offers an impedance bandwidth of 6.09 GHz (4.6 GHz–10.69 GHz).

4. RESULT AND DISCUSSION

The dielectric material used is an FR4 slab of thickness 1.5 cm. The fractal structure is fabricated from an FR4 material using a high precision abrasive water jet machine. The conventional CDRA has a resonant frequency of 3.8 GHz. It can be observed that when the fractal is applied on CDRA, the resonant frequency is shifted towards higher frequency. The resonant frequency of a DRA depends on radius 'a', height 'h' and dielectric constant of material (ε_r) (i.e., Dielectric resonator material dimensions and properties) [18].

The Lumped element circuit of a conventional CDRA is equivalent to a parallel RLC resonator. Resonant frequency of parallel resonator

$$\omega_0 = \frac{1}{\sqrt{LC}} \tag{5}$$

where, L represents the inductance and C the capacitance of the resonator. Lowering the value of L and C increases the resonant frequency of resonator. Under equilibrium condition, the time average electric energy and magnetic energy inside the resonator are the same. Variation in the structure of DRA changes its electric and magnetic fields, due to change in reactive elements [19].

Average electric energy stored in the capacitor [19] is given as follows:

$$W_e = \frac{1}{4} |V|^2 C \tag{6}$$

Average electric energy stored in the inductor [19] is given as follows:

$$W_m = \frac{1}{4} |V|^2 \frac{1}{\omega^2 L} \tag{7}$$

Implementing Koch snowflake configuration on cylindrical dielectric resonator causes material perturbation on the walls or sides. The shifting of resonant frequency is due to the inward perturbation created on the edges of the dielectric resonator. From Figure 16, let V_0 and S_0 be the volume and surface area of the conventional CDRA, V and S be the volume and surface area of Koch snowflake first iteration, i.e., cylindrical resonator after inward perturbation and Δv and Δs be the volume and surface area of the inward perturbation [20–22].

Let $\omega_0, \vec{E}_0, \vec{H}_0$ be the resonant frequency and field of conventional CDRA before perturbation, which satisfies Maxwell's equations [20, 21],

$$\nabla \times \vec{E}_0 = i\omega_0\mu\vec{H}_0 \tag{8}$$

$$\nabla \times \vec{H}_0 = -i\omega_0\varepsilon\vec{E}_0 \tag{9}$$

The Koch snowflake first iteration is applied on the conventional CDRA with ω is the modified resonant frequency and $\vec{E}, \vec{H}$ are the electric and magnetic fields of Koch snowflake first iteration, satisfies Maxwell's equation,

$$\nabla \times \vec{E} = i\omega\mu\vec{H} \tag{10}$$

$$\nabla \times \vec{H} = -i\omega\varepsilon\vec{E} \tag{11}$$

The approximate value of change in resonant frequency $(\omega - \omega_0)$ after perturbation is given by [20],

$$\omega - \omega_0 = -i\frac{\oiint_{\Delta s} \vec{E} \times \vec{H}_0^* \cdot d\vec{s}}{\iiint_{V_0} \left(\varepsilon\vec{E} \cdot \vec{E}_0^* + \mu\vec{H} \cdot \vec{H}_0^* \right) dV} \tag{12}$$

The numerator represents the perturbed surface of surface area Δs while the denominator represents the volume integration, including perturbed and unperturbed volume, $V_0 = V + \Delta V$. $\vec{E}_0^*$ and $\vec{H}_0^*$ are the complex conjugates of $\vec{E}_0$ and $\vec{H}_0$.

Now assume that perturbation is very small, $\vec{E}$ and $\vec{H}$ can be replaced by their perturbed values $\vec{E}_0$ and $\vec{H}_0$ to obtain approximate values for the change in resonant frequency [20],

$$\omega - \omega_0 = -\mathrm{i} \frac{\oiint_{\Delta s} \vec{E}_0 \times \vec{H}_0^* \cdot d\vec{s}}{\iiint_{V_0} \left(\varepsilon \left| \vec{E}_0 \right|^2 + \mu \left| \vec{H}_0 \right|^2 \right) dV} \tag{13}$$

$$\omega - \omega_0 = \omega_0 \frac{\iiint_{\Delta V} \left(\mu \left| \vec{H}_0 \right|^2 - \varepsilon \left| \vec{E}_0 \right|^2 \right) dV}{\iiint_{V_0} \left(\mu \left| \vec{H}_0 \right|^2 + \varepsilon \left| \vec{E}_0 \right|^2 \right) dV} \tag{14}$$

$$\omega - \omega_0 = \omega_0 \frac{\Delta W_m - \Delta W_e}{W_{m-W_e}} \tag{15}$$

The denominator represents the unperturbed total energy, and the numerator represents the difference between electric energy (ΔW_e) and magnetic energy (ΔW_m) removed after inward perturbation. If the perturbation is made at the place of large magnetic field, the resonant frequency is raised. Otherwise, if the perturbation is made at the place of large electric field, resonant frequency is lowered [20]. It can be inferred from Equations (14) and (15).

Fractal ring DRA has a higher resonant frequency than the fractal DRA. The shift in resonant frequency of the fractal ring is due to material perturbation inside the cavity. The change in resonant frequency after inward perturbation inside the DRA is given by [20, 21],

$$\omega - \omega_0 = \omega_0 \frac{\iiint_{\Delta V} \left(\left[\left(\Delta \overline{\overline{\mu}} \cdot \vec{H} \right) \cdot \vec{H}_0^* + \left(\Delta \overline{\overline{\varepsilon}} \cdot \vec{E} \right) \cdot \vec{E}_0^* \right] \right) dV}{\iiint_{\Delta V} \left(\mu \vec{H} \cdot \vec{H}_0^* + \varepsilon \vec{E} \cdot \vec{E}_0^* \right) dV} \tag{16}$$

where, $\Delta \varepsilon$ and $\Delta \mu$ represent the differences between permittivity and permeability of perturbed and unperturbed dielectric resonators.

$$\frac{\omega - \omega_0}{\omega} = -\frac{\Delta W_m + \Delta W_e}{W_{m-W_e}} \tag{17}$$

The denominator represents unperturbed total energy inside the resonator, and numerator represents an increase in electric and magnetic energies caused by cavity perturbation. From Equation (16) it is evident that decreasing the value of permittivity or permeability of material inside the DRA increases the resonant frequency of DRA. In fractal ring DRA a sample is inserted into the resonator with permittivity, ($\varepsilon_r = 1$), which is less than the permittivity of the material. This change in permittivity shifts the resonant frequency. If the permittivity of sample is higher than the permittivity of material, resonant frequency is lowered and vice versa [23].

Quality factor (Q-factor) is a figure of merit and the measure of bandwidth. The bandwidth of the antenna is increased by lowering the Q-factor of the resonator. Increasing surface area of DRA is another way to reduce the quality factor. The surface area of DRA can be increased by creating perturbation on the DRA. Applying Koch snowflake fractal on CDRA changes the cross section of the DRA. It increases the surface area, which increases the surface area to volume ratio (S/V), thus lowering the Q-factor and improving the bandwidth. The fractal ring decreases the permittivity inside the cavity by material perturbation [24].

Fractal ring DRA covers more surface area than conventional ring DRA and the fractal DRA. The increase in S/V ratio of the Koch snowflake fractal DRA by the implementation of fractal ring decreases the quality factor and increases the bandwidth of DRA [24, 25].

Figure 17 shows the fabricated prototype of the proposed half split fractal ring shaped DRA. The DRA has been kept on a ground plane with dimension $W \times L$ ($10 \, \mathrm{cm} \times 10 \, \mathrm{cm}$), equivalent to the dimensions of DRA discussed in Figure 2. The DRA is excited by a co-axial probe kept in the identical position as the fractal ring DRA ($d = 0.35 \, \mathrm{cm}$), discussed in Figure 8(b). The dimensions of the half split fractal DRA are similar to that discussed in Figure 12.

Figure 18 shows the simulated and measured S_{11} plots of the proposed configuration. It is noted that the measured results show the bandwidth of 7.7 GHz (90%) ranging from 4.7 GHz–12.4 GHz. The difference in the results is mainly due to the fabrication tolerances such as small air gaps between the slabs of the DRA, air gaps between the DRA and the ground plane, imperfections while drilling the hole for probe insertion.

Figure 19 demonstrates the radiation pattern in two orthogonal planes (i.e., $\emptyset = 0°$ and $\emptyset = 90°$). The co-polar and cross-polar radiation patterns of the proposed structure at different resonant

Figure 17. Fabricated proposed antenna configuration.
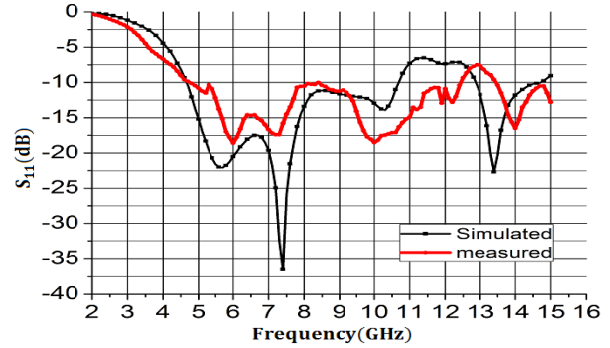

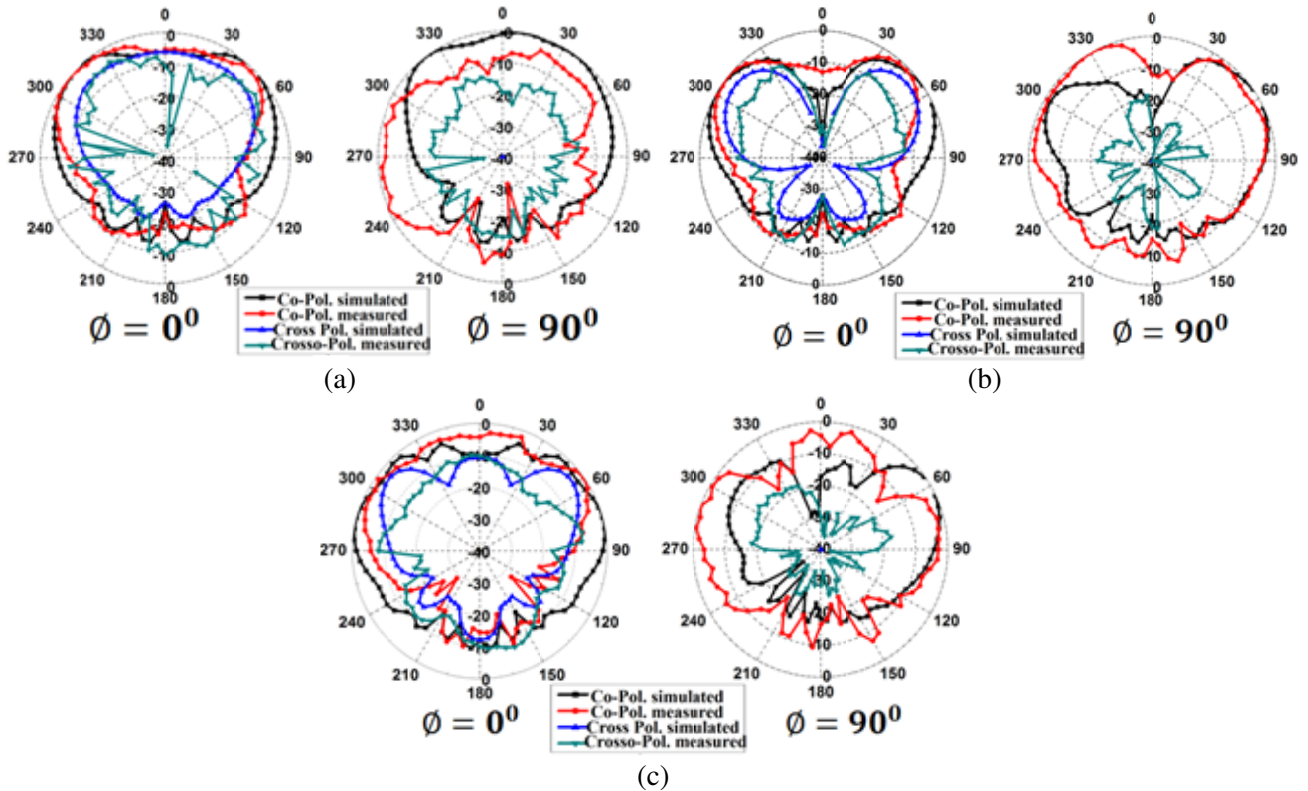**Figure 18.** Simulated and measured S_{11} plot of proposed DRA.

(a)

(b)

(c)

Figure 19. Simulated and measured normalized radiation patterns of co-polarization and cross-polarization of the proposed antenna. The radiation pattern is measured for $\emptyset = 0°$ and $\emptyset = 90°$ at (a) 6 GHz, (b) 7.4 GHz, (c) 10 GHz.

frequencies 6 GHz, 7 GHz, 10 GHz are measured. It is evident that at $\emptyset = 90°$ the cross-polar levels are very low. The null in the broadside direction of the radiation pattern at 7 GHz confirms the mode predicted for the proposed antenna geometry as $TM_{01\delta}$ like mode. But at 6 GHz the radiation pattern does not have a perfect null in the broadside direction. The radiating mode of the proposed DRA is a combination of more than single modes due to the change in geometry. The radiation pattern of the proposed DRA is varied over the bandwidth of operation. The gain of the proposed antenna is varied. So, it can be used for applications as in Cellular Communication Repeaters, LANs, and Vehicular Communication, where the mobile equipment can readily select the beam width and gain most appropriate for each antenna [26, 27].

Figure 20 shows the measured gain and efficiency as a function of frequency. It can be noted that the peak gain is obtained at resonant frequency 10 GHz which is 8.76 dBi. It can also be seen that the antenna efficiency is more than 78% of the impedance bandwidth. The maximum radiation efficiency observed at 7.4 GHz is 86%.
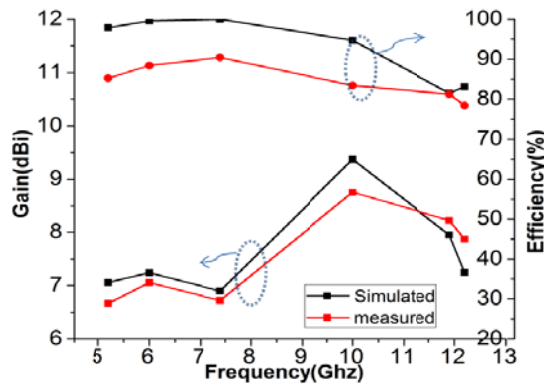

Figure 20. Gain and efficiency plot.

The antenna radiation efficiency related to antenna gain [28],

$$\eta = \frac{D}{G} \tag{18}$$

G is the measured gain of the antenna. The gain of the antenna calculated by using two-antenna method. D is the directivity calculated.

The Directivity of the antenna,

$$D = \frac{41253}{\theta_e * \theta_h} \tag{19}$$

where θ_e and θ_h are the 3 dB beamwidth of the radiation pattern of DRA along the two planes (i.e., $\emptyset = 0°$ and $\emptyset = 90°$).

Table 1 summarizes the performance characteristics of conventional CDRA with the Koch snowflake fractal, fractal ring and the proposed configuration. The conventional CDRA has an S/V ratio of 1.41, while the half split fractal ring DRA has 4.51. The bandwidth of DRA increases with the increase in S/V ratio. From Table 1, it can be inferred that the volume of CDRA is decreased by 76.63%, and the proposed DRA has a volume of 7.91 cm^3. From Table 1, it is clear that Koch snowflake DRA has higher resonant frequency than CDRA. The shift in resonant frequency is due to the cavity perturbation created on the edges of CDRA by the application of Koch snowflake fractal. With increasing number of iterations, the resonant frequency of DRA also increases. This is due to the difference in volume of the two iterations. Fractal ring causes inward cavity material perturbation inside the DRA, which reduces the effective permittivity of DRA, thus the resonant frequency of DRA is shifted. It is well understood from Table 1 that with increasing the S/V ratio, the gain of the antenna also increases.

Table 1. Comparison of the proposed antenna with the simulated geometries.

Geometry	f_r	BW	G	S	V	S/V
Conventional CDRA	3.8	15	4.8	47.82	33.85	1.41
Koch snowflake Iteration 1	6.04	57.2	5.90	40.73	18.98	2.15
Koch snowflake Iteration 2	4.57	57.57	6.56	51.5	21.09	2.44
Fractal Ring (snowflake iteration 2)	6.14	74.23	7.6	66.71	15.83	4.21
Half split fractal ring	6	90	8.76	35.7	7.91	4.51

f_r — First resonant frequency (GHz), BW — Bandwidth (%), G — Gain in dBi, S — Total surface area (cm^2), V — Volume (cm^3), S/V — Surface area to volume ratio (cm^{-1}).

5. CONCLUSION

This paper presents a novel compact half split fractal annular ring DRA. Three separate DRA geometries have been discussed. Each has been designed, analyzed and modified, followed by comparison of its performance with conventional CDRA. A Koch snowflake structure is implanted on the CDRA. The parametric studies are carried out for Koch snowflake on the CDRA. Optimized second iteration of the fractal geometry offers better performance, a bandwidth of 57.5% with a gain of 6.56 dBi. Further, the fractal ring offers a wide impedance bandwidth of 74.23% with a gain of 7.6 dBi. The structure is made compact by removing a half portion of the fractal ring without affecting its characteristics. The proposed configuration provides 90% impedance bandwidth in the range of 4.7 GHz–12.4 GHz. Experimental results prove that the proposed DRA achieves high peak gain of 8.76 dBi. The bandwidth of the antenna is increased by the reduction of Q-factor caused by material cavity perturbation by the snowflake fractal. To the best of our knowledge, such a geometry has neither been investigated nor been proposed in previous works.

ACKNOWLEDGMENT

REFERENCES

1. Long, S. A., M. W. McAllister, and L. C. Shen, "The resonant cylindrical dielectric cavity antenna," *IEEE Transactions on Antennas and Propagation*, Vol. AP-31, No. 3, 406–412, March 1983.
2. Petosa, A., *Dielectric Resonator Antenna Handbook*, Artech House, Norwood, MA, USA, 2007.
3. McAllister, M. W. and S. A. Long, "Rectangular dielectric resonator antenna," *IET Electronics Letters*, Vol. 19, No. 6, 218–219, Mar. 1983.
4. McAllister, M. W. and S. A. Long, "Resonant hemispherical dielectric antenna," *IET Electronics Letters*, Vol. 20, 657–659, Aug. 1984.
5. Mandelbrot, B., *The Fractal Geometry of Nature*, W. H. Freeman and Company, New York, 1977.
6. Dhar, S., R. Ghatak, B. Gupta, and D. R. Poddar, "A wideband Minkowski fractal dielectric resonator antenna," *IEEE Trans. Antennas Propag.*, Vol. 61, No. 6, 2895–2903, Jun. 2013.
7. Mukherjee, B., P. Patel, and J. Mukherjee, "Hemispherical dielectric resonator antenna based on Apollonian Gasket of circles — A fractal approach," *IEEE Trans. Antennas Propag.*, Vol. 62, No. 1, 40–47, Jan. 2014.
8. Majeed, A. H., A. S. Abdullah, K. H. Sayidmarie, R. A. Abd-Alhameed, F. Elmegri, and J. M. Noras, "Balanced dual-segment cylindrical dielectric resonator antennas for ultra-wideband applications," *IET Microwaves, Antennas and Propagation*, Vol. 9, No. 13, 1478–1486, 2015.

9. Ozzaim, C., F. Üstüner, and N. Tarim, "Stacked conical ring dielectric resonator antenna excited by a monopole for improved ultra-wide bandwidth," *IEEE Trans. Antennas Propag.*, Vol. 61, No. 3, Mar. 2013.

10. Sharma, A. and R. K. Gangwar, "Hybrid two segments ring dielectric resonator antenna for ultra wideband application," *International Journal of RF and Microwave Computer-Aided Engineering*, Vol. 26, No. 1, 47–53, Jan. 2016.

11. Guha, D., B. Gupta, and Y. M. M. Antar, "Hybrid monopole DRAs using hemispherical/conical-shaped dielectric ring resonators: Improved ultra wideband designs," *IEEE Trans. Antennas Propag.*, Vol. 60, 393–398, 2012.

12. Majeed, A. H., A. S. Abdullah, K. H. Sayidmarie, R. A. Abd-Alhameed, F. Elmegri, and J. M. Noras, "Compact dielectric resonator antenna with band-notched characteristics for ultra-wideband applications," *Progress In Electromagnetics Research C*, Vol. 57, 137–148, 2015.

13. Gangwar, R. K., S. P. Singh, and D. Kumar, "A modified fractal rectangular curve dielectric resonator antenna for WiMAX application," *Progress In Electromagnetic Research C*, Vol. 12, 37–51, 2010.

14. Addison, P. S., *Fractals and Chaos — An Illustrated Course*, IoP Publishing, Institute of Physics, 1997.

15. Barnsley, M. F., *Fractals Everywhere*, 2nd edition, Morgan Kaufmann, 2000.

16. Zhu, Z. W. and B. G. Jia, "On the lower bound of the Hausdorff measure of the Koch curve," *Acta Mathematica Sinica*, Vol. 19, No. 4, 715–728, Oct. 2003.

17. Kajfez, D., A. W. Glisson, and J. James, "Computed modal field distribution for isolated dielectric resonators," *IEEE Trans. Microwave Theory Tech.*, Vol. 32, 1609–1616, Dec. 1984.

18. De Medeiros, J. L. G., W. C. de Araújo, A. G. d'Assunção, L. M. de Mendonça, and J. B. L. de Oliveira, "Investigation on ZPT ceramics applied as dielectric resonator antenna for ultra-wideband systems," *Microwave and Optical Technology Letters*, Vol. 55, No. 6, 1352–1355, Jun. 2013.

19. Pozar, M., *Microwave Engineering*, 2nd edition, John Wiley & Sons, 2004.

20. Kong, J. A., *Electromagnetic Wave Theory*, Wiley Interscience, 1990.

21. Harrington, R. F., *Time Harmonic Electromagnetic Fields*, IEEE Press, New York, 2001.

22. Waldron, R. A., "Perturbation theory of resonant cavities," *Proc. IEE — Part C Monogrraphs*, Vol. 107, 272–274, 1960.

23. Chaudhary, R. K., K. V. Srivastava, and A. Biswas, "Multi-band cylindrical dielectric resonator antenna using permittivity variation in azimuth direction," *Progress In Electromagnetics Research C*, Vol. 59, 11–20, 2015.

24. Babik, G. B., C. Di Nallo, and A. Faraone, "Multimode dielectric resonator antenna of very high permittivity," *IEEE Antennas and Propagation Society International Symposium*, Vol. 2, 1383–1386, Monterey, CA, 2004.

25. Mongia, R. K. and P. Bhartia, "Dielectric resonator antennas — A review and general design relations for resonant frequency and bandwidth," *Int. J. of Microwave Millimeter-Wave Eng.*, Vol. 4, No. 3, 230–247, Jul. 1994.

26. Wannagot, G. A., A. Macqueen, R. E. Cozzolino, and L. J. Reading, "Variable gain and variable beam width antenna (the hinged antenna)," U.S. patent 6774854 B2, Aug. 10, 2004.

27. Mohebbi, B. B., "Variable gain antenna for cellular repeater," U.S. patent 20080299897 A1, Dec. 4, 2008.

28. Balanis, C. A., *Antenna Theory, Analysis and Design*, 3rd edition, Wiley, New York, NY, USA, 2005.